Progress In Electromagnetics Research M, Vol. 139, 69–81, 2026 PIER M

(Received 6 June 2026, Accepted 15 July 2026, Scheduled 17 August 2026)

A Dual-Split Ring Resonator Based Microwave Sensor for Simultaneous Permittivity and Permeability Characterization

Yusnita Rahayu[1,*], Evelyn D. Amanda[1], and Yohanes G. Adhiyoga[2]

[1]Department of Electrical Engineering, Universitas Riau, Pekanbaru, Indonesia
[2]Research Center for Telecommunication, National Research and Innovation Agency (BRIN), Bandung, Jawa Barat, Indonesia

ABSTRACT: Accurate characterization of magnetodielectric materials is required for the development of microwave sensors and high-frequency communication systems. This study proposes a compact planar microwave sensor that uses a single dual-Split-Ring Resonator (SRR) to simultaneously measure permittivity and permeability. The core innovation lies in the spatial segregation of electric-field-dominant and magnetic-field-dominant sensing regions within a unified resonator framework, which effectively suppresses mutual interference between the dielectric and magnetic sensing channels. Designed to resonate at 4.15 GHz, the sensor's performance was evaluated through full-wave electromagnetic simulations and experimental validation using six different materials under test (MUT) (including Magtrex555 and various Rogers's substrates). Sixty independent measurements were conducted to ensure reliability. The experimental results demonstrate high sensitivity, with 144.2 MHz/ε_r for permittivity and 45.4 MHz/μ_r for permeability. The proposed sensor enables characterization across a measured permittivity range of 2.2–6.5 and a permeability range of 1–6, demonstrating its capability to evaluate both dielectric and magnetic properties within the specified measurement domain. The proposed sensor achieved average characterization accuracies of 96.93% and 98.81% for permittivity and permeability, respectively, with minimum errors as low as 0.03%. These results confirm that dual-SRR architecture provides a robust, repeatable, and non-destructive solution for magnetodielectric material characterization with a highly compact form factor.

1. INTRODUCTION

In recent years, the advancement of electromagnetic and telecommunication technologies has been closely associated with progress in material research. Particular attention has been directed toward magnetodielectric materials characterized by relatively high permittivity (ε_r) and permeability (μ_r). The electromagnetic properties of a material can be characterized by analyzing high-frequency response variations on an appropriate sensing platform [1, 2]. Owing to these properties, such materials have been extensively used in antenna systems, microwave sensors, and wireless communication applications. In recent years, interest in material dielectric and magnetic characterization has increased remarkably for numerous applications in different fields, such as industry [3, 4], agriculture [5], chemistry [6, 7], healthcare [8, 9], and others [10–14]. Many sensing techniques have been proposed for these applications and can be generally categorized into non-resonant and resonant methods. Numerous new materials have been introduced in the microwave region and are widely used for applications such as microwave shielding, microwave absorbers [15], and microwave sensors [16]. There, precise characterization of electromagnetic parameters is critical because variations in ε_r and μ_r directly affect the resonance characteristics, impedance matching conditions, operational bandwidth, and overall system performance at microwave frequencies. To address this requirement, various material characterization techniques have been developed, one of which is the transmission line method, which is widely used to measure electromagnetic material properties [17, 18]. Recent studies on SRR-based sensors have also been proposed for the characterization of liquid permittivity, including a meander-, ladder-, and T-shaped resonator sensor designed for aqueous solution analysis [19], as well as a symmetric bar-chart-shaped resonator that achieves a high Q-factor for fluid permittivity measurements [20]. Although these approaches highlight the versatility of SRR-based structures in permittivity sensing applications, they are predominantly limited to liquid samples and do not consider the simultaneous characterization of permeability, which represents the primary focus of this study. Specifically, for magnetodielectric materials, the simultaneous fluctuation of both ε_r and μ_r poses a major hurdle, as the perturbation from one parameter can frequently 'mask' or be misinterpreted as a variation in the other, thereby demanding a sensing mechanism that can effectively decouple these two electromagnetic responses.

Among various planar microwave sensing structures, SRRs have attracted significant attention due to their compact size and superior sensitivity. Compared with conventional quarter-wavelength transmission-line resonators, SRRs offer enhanced sensing performance while occupying a smaller footprint, particularly at lower microwave frequencies [19]. Its popularity can be attributed to its compact physical dimensions, distinct resonance features, and strong resonant behavior. Conventional SRR configurations exhibit dominant sensitivity to mag-

* Corresponding author: Yusnita Rahayu (yusnita.rahayu@lecturer.unri.ac.id).

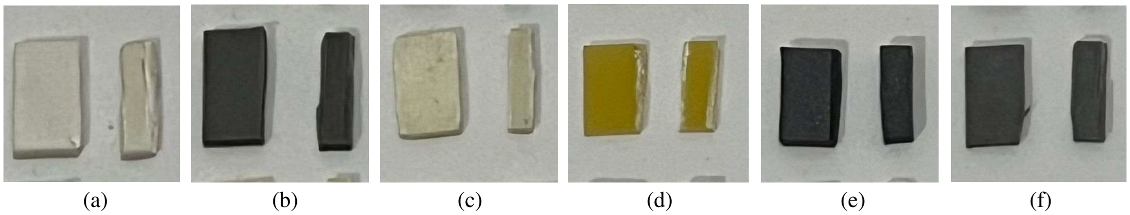

FIGURE 1. Samples of MUT in the proposed sensor: (a) Rogers 4003C, (b) Rogers 5880, (c) Rogers 4350B, (d) FR-4, (e) Magtrex555, and (f) Rogers 5870.

netic field components perpendicular to the resonator plane, making them well-suited for permeability measurements. The predominance of the magnetic field results in a disparity in sensing performance, as sensitivity to permittivity variations is relatively diminished. Consequently, achieving simultaneous, accurate extraction of ε_r and μ_r becomes more difficult, particularly for magnetodielectric materials in which the electric and magnetic properties vary simultaneously. Recent work by [22] demonstrated that a microstrip sensor based on a complementary split-ring resonator (CSRR)-derived structure is capable of comprehensively characterizing magnetodielectric materials, such as Fe_3O_4-PDMS, by spatially separating the electric and magnetic sensing regions within a single device. Although [22] also employs spatially separated sensing regions, its design is based on a CSRR-inspired structure etched on the ground plane, which is fundamentally different from the conventional SRR configuration adopted in this study, where the dual-SRR resonators are directly excited via coupling with the microstrip line. This structural difference provides a simpler excitation scheme and facilitates more localized field confinement, while retaining the benefit of spatial separation between sensing regions. By concentrating the electric and magnetic fields in distinct areas of the sensor, the ε_r and μ_r of the material can be independently extracted with minimal cross-interference.

Several approaches have been reported to address this issue. They include CSRRs [23] and multi-resonator and multi-mode sensing configurations. Although improved dual-parameter sensitivity has been demonstrated, these approaches typically require more complex structures, additional sensing regions, or separate resonance modes to achieve this improvement. These factors reduce their suitability for compact, low-cost, planar microwave sensor designs. Furthermore, multi-mode or multi-resonator sensing strategies frequently encounter technical challenges such as overlapping and difficulties in frequency alignment, which can lead to significant inaccuracies during the simultaneous extraction of permittivity and permeability.

Despite these developments, the reliable and independent extraction of permittivity and permeability using a single planar sensor structure remains challenging. Achieving a balanced response to both electric and magnetic field perturbations while preserving structural simplicity remains unresolved. This condition motivates the development of a sensing architecture that enables spatial separation between regions dominated by electric and magnetic fields within a unified resonator structure.

In this study, a dual-SRR-based microwave sensor is proposed for magnetodielectric material characterization. The proposed dual-SRR leverages its inherent geometric symmetry to isolate the electric-field hotspot at the split gaps while confining the magnetic field within the loops, thereby preventing cross-parameter interference. Full-wave electromagnetic simulations were performed using the Computer Simulation Technology (CST) Microwave Studio to examine the resonant behavior and S_{21}. Various MUT, including real materials such as FR-4, Rogers 5870, Rogers 4003C, Rogers 5880, and Rogers 4350B, are considered in this work. Unlike previous studies that rely on complex multi-resonators or multi-mode configurations, this work introduces a cohesive single-layer dual-SRR framework. The main contributions include: 1) A compact design achieving spatially segregated sensing zones for balanced ε_r and μ_r sensitivity; 2) A systematic suppression of mutual interference enabling independent parameter extraction; and 3) Experimental validation demonstrating a high average accuracy of over 96%, providing a robust solution for real-time magnetodielectric characterization. This approach reduces the structural complexity while maintaining high sensitivity and measurement repeatability.

2. WORKING PRINCIPLES OF THE PROPOSED SENSOR

The proposed microwave sensor is designed based on a planar dual-SRR configuration concept introduced in [21] to achieve balanced sensitivity to both electric- and magnetic-field perturbations. The sensor was implemented on a Rogers 5880 substrate with a relative permittivity of $\varepsilon_r = 2.2$, a thickness of $h = 1.57$ mm, and a loss tangent of 0.0009. The substrate was selected because of its low dielectric loss and stable electromagnetic properties at microwave frequencies.

The substrate samples used as MUT are shown in Fig. 1. As illustrated in Figs. 1(a)–(f), the investigated materials include Rogers 5870, Rogers 4003C, Rogers 4350B, FR-4, Magtrex555, and Rogers Duroid 5880. Six substrate samples with identical dimensions were fabricated for each substrate type and measured independently to ensure consistent results.

For permittivity characterization, each sample was prepared with dimensions of 10 mm $\times$ 5 mm, whereas samples used for permeability characterization measured 10 mm $\times$ 2 mm. The thickness of each sample corresponded to the original substrate specifications of the respective MUT. This approach was adopted to enhance the measurement repeatability and reduce uncertainty. It aligns with findings reported in previous cross-sensitivity studies, in which measurement accuracy was observed to deteriorate when the dimensions of the tested sample deviate from the designated sensing region [25]. This further reinforces the importance of matching MUT dimensions to the sensing area to ensure reliable measurement results.

Prior to measurement process, the Libre Vector Network Analyzer (VNA) was calibrated using the standard short-open-load-through (SOLT) procedure over the operating frequency range of interest to minimize systematic measurement errors. All measurements were carried out under controlled laboratory conditions with an ambient temperature of approximately 25 ± 2°C and a relative humidity of $60 \pm 5\%$. During the measurement process, the samples were consistently positioned within the designated sensing region using alignment references to reduce placement errors, and the corresponding S_{21} responses were recorded for each substrate sample. In addition, repeated measurements were performed to evaluate the repeatability of the sensing system. These precautions help mitigate experimental uncertainties and improve the reliability of reported results.

The measurement procedure began by connecting the Libre VNA to a laptop via a USB Type-C interface. Subsequently, the fabricated microwave sensor was connected to ports 1 and 2 of the Libre VNA via SMA connectors and coaxial cables, as shown in Fig. 2.

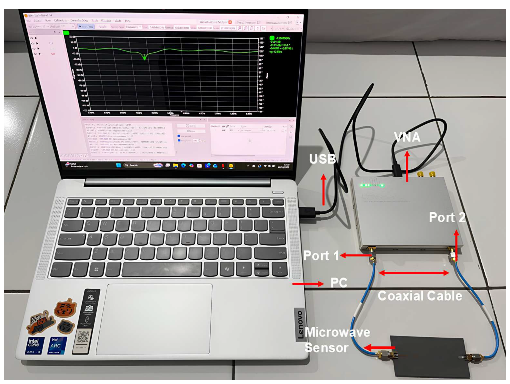

FIGURE 2. Measurement procedure of the proposed sensor.

3. NUMERICAL MODELING AND SENSOR CHARACTERIZATION

The proposed microwave sensor comprises two identical SRRs arranged symmetrically along a central microstrip transmission line, as shown in Fig. 3. Each resonator consists of a narrow split gap and a conductive loop, which collectively form an equivalent LC resonant circuit through their capacitive and inductive effects. The dual-SRR geometry was intentionally designed to generate spatially separated sensing regions, enabling an independent interaction of the electric and magnetic fields with the MUT while maintaining a compact, low-complexity structure.

In particular, the split-gap regions concentrate the electric field and serve as an electric-field-dominant sensing area for permittivity characterization, whereas the resonator loops support strong circulating currents, which produce a magnetic-field-dominant sensing area for permeability characterization. The optimized geometric parameters and dimensions of the proposed sensor are presented in Table 1.

TABLE 1. Structure of the proposed sensor with dimensions.

Parameter	Dimension (mm)
L_1	40
L_2	80
L_3	12.50
L_4	2.52
L_5	32
L_6	4.95
L_7	10
L_8	0.60
L_9	1.20

3.1. Surface Current and Equivalent Circuit Characteristic

The SRR consists of a metallic ring with a narrow split that behaves as an equivalent LC tank circuit. Under resonance conditions, electromagnetic energy oscillates between the magnetic field stored in the conductive loop, representing the inductive component (L), and the electric field concentrated across the split gap, representing the capacitive component (C).

The electromagnetic behavior of the proposed dual-SRR sensor is governed by the field distribution generated around the microstrip transmission line and resonant structures. Fig. 4(a) shows the electric-field (E-field) distribution, and Fig. 4(b) presents the magnetic-field (H-field) distribution at the resonant frequency of 4.084 GHz. As shown in Fig. 4(b), the H-field exhibits strong localization around the outer sections of the SRR, particularly in the region farthest from the microstrip line. This indicates that the SRR primarily interacts with the magnetic component of the guided wave, producing strong H-field confinement that drives the resonance mechanism. Conversely, the E-field distribution in Fig. 4(a) remains minimal in the same region, confirming the negligible E-field coupling experienced by the SRR. This separation of the dominant H-field and weak E-field illustrates the magnetic-field sensitive nature of the resonator, enabling selective perturbation when a magnetodielectric material is placed near the resonant region. The high isolation between sensing regions is attributed to the optimized distances $L7$ and $L8$, which ensure that the displacement currents in the split gap do not significantly perturb the magnetic flux induction within the outer loops.

The field confinement around the SRR results from the induced circulating surface currents along the metallic ring, which generate a loop-like magnetic flux that reinforces the H-field concentration. These surface currents constitute the primary inductive component of the resonant structure, and the split gap provides an effective capacitance. The interaction between the inductive loop and capacitive gap creates a localized LC resonance, in which the magnetic energy stored in the current loop alternates with the electric energy stored across the split area. This mechanism produces a highly confined near-field distribution, making the sensor particularly sensitive to small perturbations in the electromagnetic properties of materials placed within the field-interaction zones. The capacitive split gap exhibits strong E-field concentration, making this region highly sensitive to variations in relative permittivity. In

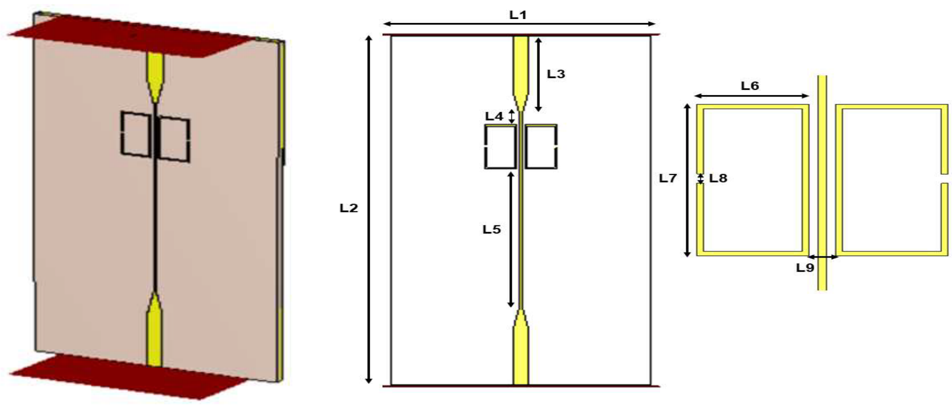

FIGURE 3. Structure of the proposed sensor with dimensions.

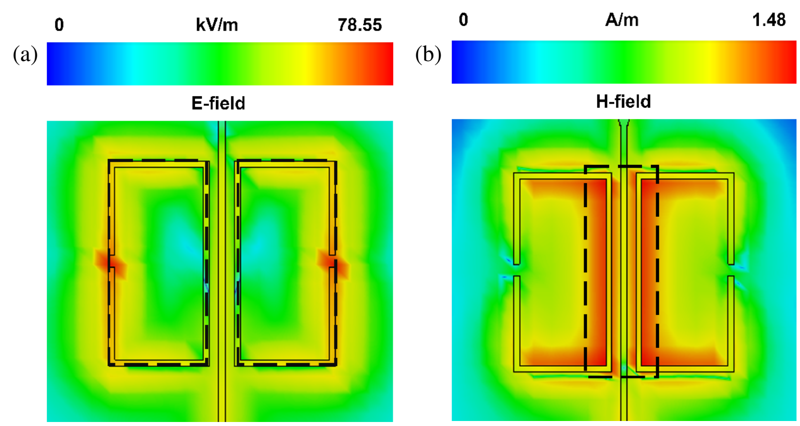

FIGURE 4. Simulated electromagnetic field distributions at the resonant frequency of $= 4.084$ GHz. (a) Electric field distribution and (b) magnetic field distribution of the proposed dual-SRR sensor.

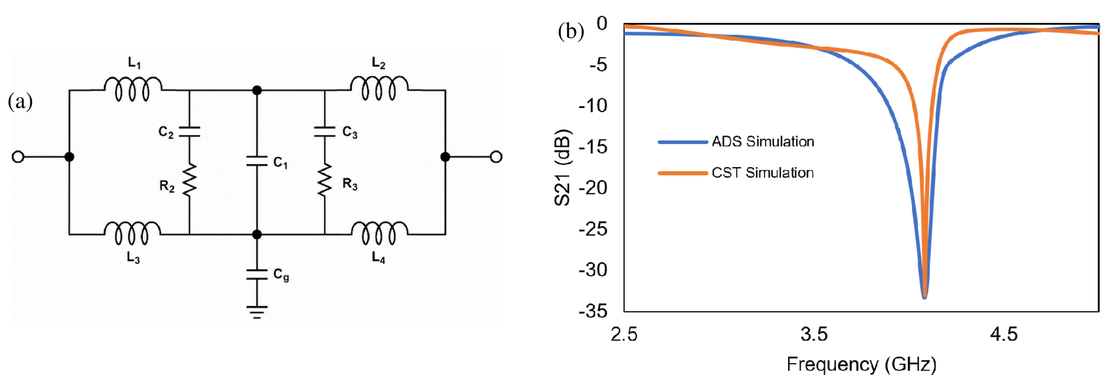

FIGURE 5. (a) Equivalent Circuit (EQC) for proposed sensor and (b) ADS vs CST simulation.

contrast, the outer conductive loop supports the confinement of an intense.

The H field is generated by circulating surface currents, enabling enhanced sensitivity to relative permeability variations. This spatial field separation allows independent perturbation of the dielectric and magnetic properties within a single planar resonator structure.

Figure 5(a) shows the equivalent circuit of the proposed dual-SRR sensor, and Fig. 5(b) demonstrates the good agreement between the advanced design system (ADS) and CST simulations, confirming the validity of the model at approximately 3.9 GHz. The electromagnetic behavior of the proposed dual-SRR sensor can be represented by a lumped element equivalent circuit. The circuit incorporates two terminal ports (Term 1 and Term 2), each with a characteristic impedance of $50\,\Omega$, interconnected via two microstrip transmission lines (TL_1 and TL_2) with a width of $W = 4.95$ mm and length of $L = 2.5$ mm. Each individual SRR element was modeled using an inductor ($L_1 = L_2 = 15$ nH), a split-gap capacitor ($C_2 = C_3 = 0.101$ pF), and an ohmic loss resistor ($R_1 = R_2 = 3.7\,\Omega$). The electromag-

(a) (b) (c)
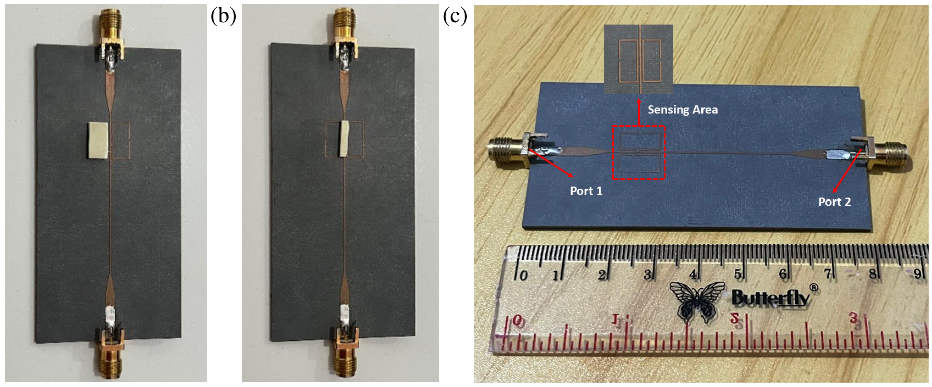

FIGURE 6. Fabricated prototype of the proposed sensor with the placement of MUT: (a) Sensitivity of permittivity and (b) sensitivity of permeability, and (c) fabrication of the proposed sensor.

netic interaction between the two SRR elements is captured by a coupling capacitor $C_1 = 1.8\,\text{pF}$ positioned at the center of the circuit, and C_g represents the grounding capacitance of the structure. The overall symmetric topology of the circuit closely replicates the sensor's physical layout, in which each SRR functions independently but remains electromagnetically coupled to the other through capacitive interaction.

The resonant behavior of the proposed sensor can be approximated using an equivalent LC resonator model. The resonant frequency is determined using the following Eq. (1):

$$f_r = \frac{1}{2_\pi \sqrt{LC}} \tag{1}$$

Because the MUT acts as a capacitive perturbation to the resonator, the resulting resonant behavior can be analyzed using cavity perturbation theory, as given by Eq. (2) [24]:

$$\frac{\Delta f_r}{f_r} = -\frac{1}{2} \frac{\int V_p \left(\Delta_\varepsilon \left| E \right|^2 + \Delta_\mu \left| H \right|^2 \right) dv}{\int_V \left(\varepsilon \left| E \right|^2 + \mu \left| H \right|^2 \right) dv} \tag{2}$$

In (2), f_r denotes the resonant frequency of the unloaded resonator, and Δf_r represents the resonant frequency shift caused by introducing the MUT. The parameters $\Delta\varepsilon$ and $\Delta\mu$ correspond to the variations in permittivity and permeability of the MUT, respectively. The electric- and magnetic-field intensities are represented by E and H; V_p denotes the perturbation volume occupied by the MUT; and V represents the total effective volume of the resonator. According to (2), the resonant frequency shift is directly related to the variation of the electromagnetic properties of the MUT and the amount of stored electric and magnetic energy within the sensing region. The frequency decreases when either the effective permittivity or permeability increases. For the proposed sensor, the perturbation effect associated with the E field is dominant within the split-gap region, whereas the perturbation associated with the H field is dominant around the resonator loop. Due to the spatial field separation, the term $\int_V \mu |H|^2 dv$ in (2) becomes negligible in the split-gap region, allowing for a decoupled extraction of permittivity without magnetic interference. Similarly, in the resonator loop region, the term $\int_V (\varepsilon |E|^2$ becomes negligible, ensuring that the resonance shift is primarily governed by permeability variations. Consequently, dielectric and magnetic properties can be characterized independently by placing the MUT within the corresponding sensing hotspot.

4. MEASUREMENT VALIDATION

The developed sensor resonates near 4.15 GHz in the lower C-band. The chosen frequency represents an effective compromise between sensor performance and fabrication feasibility. Low-frequency operation requires larger resonators, increasing sensor size. In contrast, higher-frequency operation tends to make the resonant response more susceptible to dimensional variations and manufacturing tolerances. Consequently, the optimized frequency of 4.15 GHz provides reliable sensing performance while preserving a practical and compact sensor configuration.

4.1. Sensor Fabrication and Measurement Procedure

The transmission coefficient (S_{21}) is adopted as the primary sensing parameter due to its higher sensitivity to resonant frequency variations induced by the presence of the MUT. In the proposed resonator, the resonant response manifests itself as a pronounced and well-defined transmission dip in S_{21}, allowing more stable and accurate frequency tracking than the reflection response. Although S_{11} can also represent impedance changes, it is more affected by matching conditions and parasitic influences, which may compromise its reliability for quantitative evaluation. Since both S_{11} and S_{21} originate from the same resonant mode, S_{21} alone is considered sufficient for accurately characterizing the resonant behavior in this study.

Figure 6 illustrates the fabricated prototype and placement of the MUT in the sensing region. During the measurement process, the transmission response (S_{21}) was recorded under both unloaded and loaded conditions to extract the corresponding resonant frequency shifts.

Different MUTs were placed in the sensor regions to study how dielectric and magnetic quality affect resonant response. Each sensor had 60 measurements, 10 for each of the six substrate samples. The derived resonant frequencies for each sub-

TABLE 2. Average resonant frequency for permittivity.

MUT	ε_r	F_{min} (GHz)	F_{max} (GHz)	Avg f_{re} (GHz)
Rogers 5880	2.2	3.936	4.092	3.984
Rogers 5870	2.33	3.912	4.056	3.971
Rogers 4003C	3.38	3.666	3.896	3.777
Rogers 4350B	3.48	3.192	3.760	3.662
FR-4	4.3	3.552	3.712	3.607
Magtrex555	6.5	3.291	3.956	3.364

TABLE 3. Average resonant frequency for permeability.

MUT	μ	F_{min} (GHz)	F_{max} (GHz)	Avg f_{rm} (GHz)
Rogers 5880	1	4.13	4.15	4.143
Rogers 5870	1	4.13	4.15	4.142
Rogers 4003C	1	4.13	4.15	4.142
Rogers 4350B	1	4.13	4.15	4.143
FR-4	1	4.13	4.15	4.141
Magtrex555	6	3.916	3.916	3.916

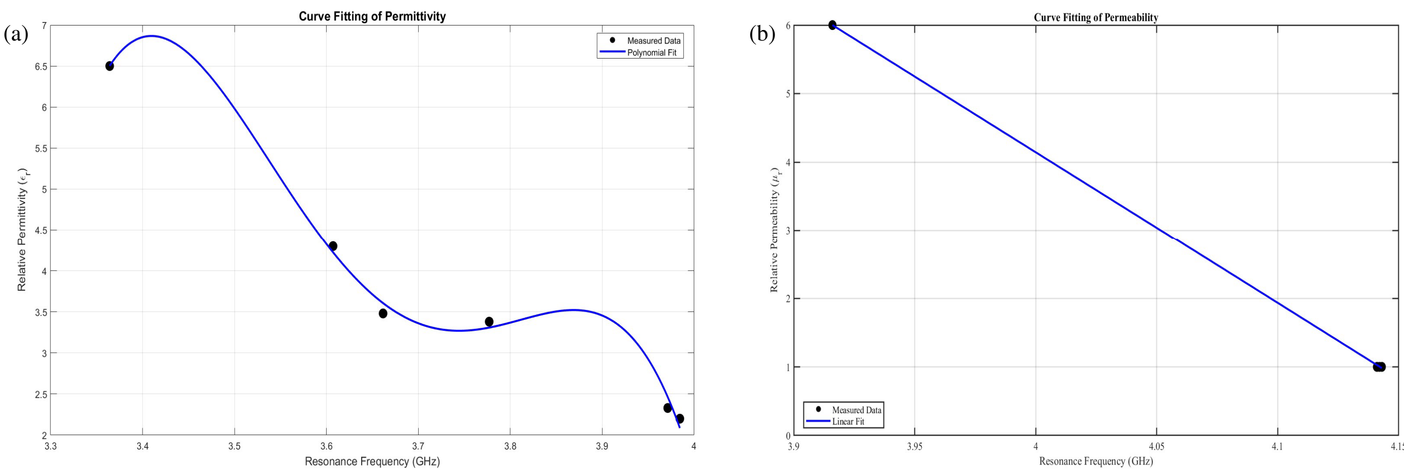

FIGURE 7. Comparison of the simulated (a) S_{21} for the permittivity-sensitive resonance based on the curve fitting and (b) S_{21} for the permeability-sensitive resonance based on the fitting curve.

strate type were averaged to reduce measurement noise and sample variability. All investigated materials' average resonant frequencies were analyzed and summarized in Tables 2 and 3.

4.2. MATLAB Curve Fitting

The MATLAB Curve Fitting Toolbox was used to develop empirical models for electromagnetic material characterization based on experimentally averaged resonant frequencies. Permittivity and permeability curve-fitting analyses were done separately. In each analysis, the average resonant frequency E field (f_{re}) and H field (f_{rm}) were the independent variables, while the related electromagnetic property (ε_r or μ_r) was forecasted.

Figure 7(a) illustrates the curve-fitting result obtained from the E-field sensing region, demonstrating the correlation between the average resonant frequency and relative permittivity of the MUT. A fourth-order polynomial function was selected as the regression model because it accurately represents the nonlinear behavior observed in the measured data. The fitted curve closely followed experimental data points, indicating a high degree of agreement between the proposed model and measurement results.

The resulting empirical relationship between the resonant frequency and relative permittivity is expressed in Eq. (3) as follows:

$$\varepsilon_r = p1 f_r^4 + p2 f_r^3 + p3 f_r^2 + p4 f_r + p5 \tag{3}$$

The resulting regression coefficients $p_1 = -493.3794$, $p_2 = 7251.1932$, $p_3 = -39908.3818$, $p_4 = 97480$, $p_5 = -89140$. The goodness-of-fit metrics confirmed the excellent performance of the proposed regression model. The fitting process yielded a low sum of squared errors (SSE) of 0.005395 and a root mean square error (RMSE) of 0.09786, indicating a minimal deviation between the fitted curve and measured data. In addition, the coefficient of determination (R^2) demonstrates a strong correlation between the predicted and measured values.

Figure 7(b) presents the regression model developed for permeability extraction, revealing the relationship between MUT permeability and its corresponding average resonant frequency. Based on the fitting analysis, a first-order polynomial (linear) model was selected to represent this relationship. The resulting fitted curve demonstrated excellent agreement with measured data points.

This observed linear relationship can be physically explained through the resonant behavior of the proposed sensing structure, in which the presence of a MUT alters the effective magnetic permeability in the resonator's high-field region.

This change consequently modifies the effective inductance of the resonant system. Since the resonant frequency is defined by $f_r \propto \frac{1}{\sqrt{LC}}$, the variation in inductance results in a measurable and approximately linear shift in the resonant frequency within the sensor's operating range.

The mathematical model presented in Eq. (4), which was derived from the curve-fitting process, is expressed as follows:

$$\mu_r = p_1 f_r + p_2 \tag{4}$$

where $p_1 = -22.1029$ and $p_2 = 92.5546$ obtained from MATLAB regression analysis. In Eq. (4), the parameter p_1 denotes the sensitivity coefficient of the sensing structure, representing the rate of change of relative permeability with respect to variations in the resonant frequency. Meanwhile, p_2 corresponds to the intercept term, which reflects the system's baseline permeability under the reference resonant condition. The linear approximation is held under a quasi-linear perturbation regime, in which the electromagnetic field distribution within the resonator remains stable, and the interaction between the MUT and the sensing region does not introduce significant nonlinear effects, such as strong field distortion or mode coupling.

The goodness-of-fit metrics indicate that the proposed model achieves strong predictive accuracy, with an RMSE of 0.0151, suggesting a very small deviation between the predicted and measured values. These results demonstrate that the proposed sensor exhibits a reliable response to variations in the relative permeability of the tested materials. This low error further validates that the proposed resonator operates within a stable electromagnetic regime, in which the dominant response is mainly governed by magnetic-field perturbations rather than radiation losses or parasitic coupling effects, thereby enabling reliable extraction of the relative permeability.

The numerical modelling findings show that empirical polynomial models can consistently correlate the resonant frequency changes induced by the two dedicated sensing structures with electromagnetic properties. Using a single-sensor platform and independent curve-fitting models for permittivity and permeability characterisation, the proposed sensing strategy uses spatially separated sensing regions and independent regression models to reduce cross-parameter interference during material property extraction.

The results demonstrate that the proposed sensing approach may estimate dielectric and magnetic characteristics from resonant frequency responses. The sensor is an effective and practical solution for electromagnetic material characterisation, and the sensing platform integrates spatially differentiated sensing regions with independent calibration equations to extract dielectric and magnetic properties.

4.3. Sensitivity Analysis

Sensitivity is a key parameter in resonance-based sensors used to assess a sensor's capability to detect variations in the electromagnetic properties of a tested material. It is defined as the magnitude of the resonant frequency shift induced by changes in the material's properties. A higher sensitivity indicates a stronger frequency response to material variations, reflecting a more pronounced electromagnetic interaction between the sensor and the MUT [27].

$$S = \frac{\Delta fr}{\Delta \varepsilon_r} \tag{5}$$

$$S = \frac{\Delta fr}{\Delta \mu_r} \tag{6}$$

Equations (5) and (6) are used to evaluate the sensor's responsiveness to variations in material properties. In this context, S represents sensitivity, and Δf_r denotes the change or difference between the highest and lowest measured resonant frequencies induced by the presence of the tested material. Meanwhile, $\Delta\varepsilon_r$ and $\Delta\mu_r$ represent the differences between the highest and lowest relative permittivity and permeability values of the tested materials, respectively.

Figure 8 shows the measured and simulated S_{21} responses of the proposed sensor under unloaded conditions. The fabricated sensor exhibited a resonant frequency of 4.15 GHz during the measurement, whereas the simulated resonant frequency was 4.08 GHz. The slight upward shift in the measured resonant frequency (4.15 GHz) compared with the simulation (4.08 GHz) is primarily attributed to fabrication tolerances of the printed circuit board (PCB) etching process and the dielectric constant

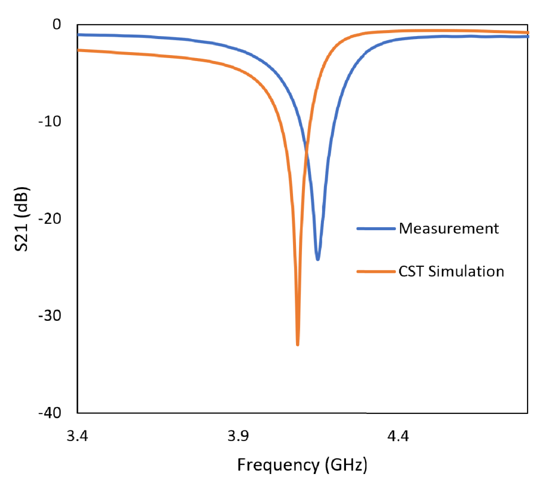

FIGURE 8. Comparison of S_{21} simulation and measurement.

tolerance of the Rogers 5880 substrate. These unloaded resonant frequencies served as reference values for evaluating resonant frequency shifts caused by the introduction of different MUTs during the characterization process. The resonant frequency shift is defined in Eq. (7):

$$\Delta f_r = f_0 - f_r \tag{7}$$

where f_0 and f_r are the unloaded and loaded resonant frequencies, respectively. f_0 denotes the resonant frequency of the sensor without the MUT, which is 4.15 GHz, and f_r represents the resonant frequency after the MUT is placed in the sensing region. The corresponding values are presented in Table 4.

TABLE 4. Resonant frequency shift results obtained from the proposed sensor for different relative permittivity values of the tested materials.

Permitivity (ε_r)	Loaded Resonance Freq. (f_r) (GHz)	Δf_r (GHz)
2.2	3.984	0.166
2.33	3.962	0.187
3.38	3.777	0.373
3.48	3.662	0.488
4.3	3.607	0.543
6.5	3.364	0.786

As presented in Table 4, the calculated frequency shift (Δf_r) increases from 166 MHz for a material with a relative permittivity (ε_r) of 2.2 to 786 MHz for a material with ε_r of 6.5. This trend indicated that higher permittivity values produced larger resonant frequency shifts, reflecting a stronger electromagnetic interaction between the MUT and the sensor. Therefore, the proposed sensor exhibits good sensitivity to variations in dielectric properties and is capable of effectively characterizing different permittivity values.

Based on the measurement results, the average permittivity sensitivity can be calculated using Eq. (5) as follows:

$$\Delta f_r = 3.984 - 3.364 = 0.620\,\text{GHz}$$

$$\Delta\varepsilon_r = 6.5 - 2.2 = 4.3$$

Therefore:

$$S_\varepsilon \frac{0.620}{4.3} = 0.1442\,\text{GHz}/\varepsilon_r$$

Normalized Sensitivity:

$$S_{n,\varepsilon} = \frac{\Delta f_r/f_0}{\Delta\varepsilon_r} \tag{8}$$

Therefore:

$$S_{n,\varepsilon} = \frac{0.620/4.15}{4.3} = 0.0347 \approx 3.47\%$$

Table 5 summarizes the frequency-shift results obtained for materials with different permeability values. The sensor produces only minor frequency shifts of 0.007–0.009 GHz for non-magnetic materials ($\mu_r \approx 1$), while a significantly larger shift of 0.234 GHz is recorded for a magnetic material with $\mu_r = 6$.

TABLE 5. Resonant frequency shift results obtained from the proposed sensor for different relative permeability values of the tested materials.

Permitivity (ε_r)	Loaded Resonance Freq. (f_r) (GHz)	Δf_r (GHz)
1	4.143	0.007
1	4.142	0.008
1	4.142	0.008
1	4.143	0.007
1	4.141	0.009
6	3.916	0.234

These results confirm the high sensitivity of the magnetic sensing region to permeability variations and demonstrate the effectiveness of the proposed sensor in distinguishing magnetic from non-magnetic materials through their resonant responses.

For the permeability analysis, the average permeability sensitivity can be determined using Eq. (6) as follows:

$$\Delta f_r = 4.143 - 3.916 = 0.227\,\text{GHz}$$

$$\Delta\mu_r = 6 - 1 = 5$$

Therefore:

$$S_\mu = \frac{0.227}{5} = 0.0454\,\text{GHz}/\mu_r \approx 45.4\,\text{MHz}/\mu_r$$

Normalized Sensitivity:

$$S_{n,\mu} = \frac{\Delta f_r/f_0}{\Delta\mu_r} = \frac{0.227/4.15}{5} = 0.01094 \approx 1.09\%$$

Based on the sensitivity analysis, the proposed sensor achieves a sensitivity of 144.2 MHz/unit for permittivity characterization and 45.4 MHz/unit for permeability characterization. These results indicate that the sensor exhibits a stronger response to variations in permittivity compared to permeability. Nevertheless, the obtained permeability sensitivity remains sufficiently significant to distinguish between magnetic and non-magnetic materials.

Equation (9) provides a sensitivity matrix that illustrates the decoupling extent between the two sensing responses. The matrix was arranged in accordance with the results of Table 4 and Table 5, which represent the varying permittivity and permeability. For a permeability of 1, the total resonant frequency variations are 0.95 MHz/unit, as indicated by the magnetic sensitivity region to permittivity. In contrast, the electric sensitivity to permeability is negligible, as the E-field distribution in Fig. 4(a) is concentrated solely in the spilt gap with a very small H-field.

$$\begin{bmatrix} \Delta f_E \\ \Delta f_H \end{bmatrix} = \begin{bmatrix} S_{E\varepsilon} & S_{E\mu} \\ S_{H\varepsilon} & S_{H\mu} \end{bmatrix} \begin{bmatrix} \Delta\varepsilon_r \\ \Delta\mu_r \end{bmatrix} \tag{9}$$

$$\begin{bmatrix} \Delta f_E \\ \Delta f_H \end{bmatrix} = \begin{bmatrix} 144.2 & \approx 0 \\ 0.95 & 45.4 \end{bmatrix} \begin{bmatrix} \Delta\varepsilon_r \\ \Delta\mu_r \end{bmatrix} \tag{10}$$

Overall, the proposed dual-SRR sensor can characterize electromagnetic properties of materials through consistent, measurable resonant frequency shifts.

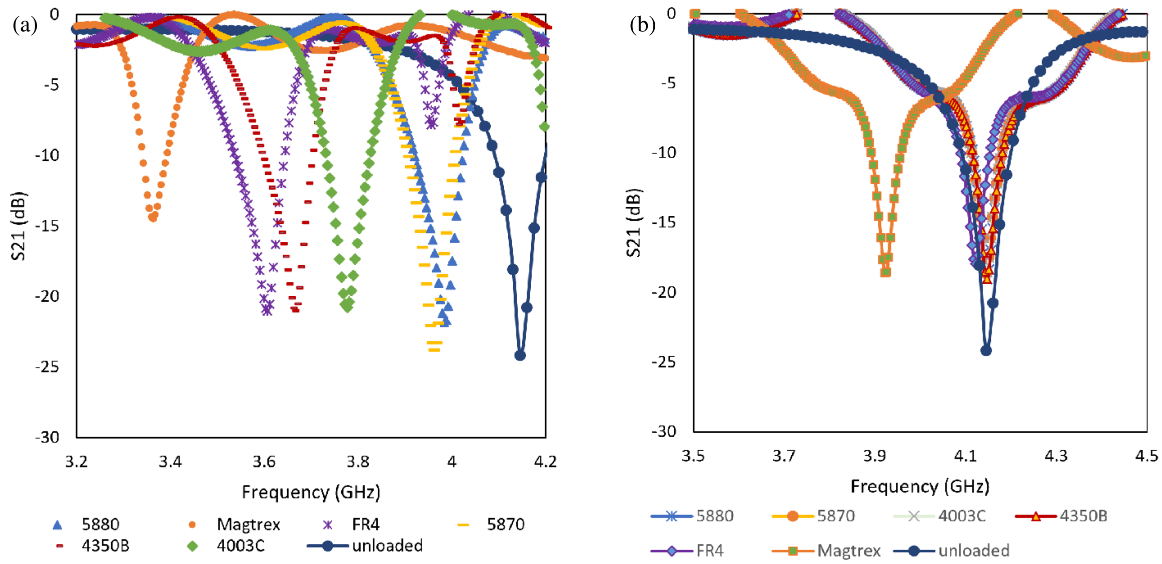

FIGURE 9. Measured S_{21} responses of the (a) E-field and (b) H-field sensing structure under unloaded conditions and with various MUT.

The proposed sensor was compared to a microstrip-line-coupled SRR sensor with a T-shaped configuration for additional evaluation. This sensor has been reported for the liquid permittivity characterisation of human milk samples at 6 GHz [26]. That design obtained a normalised sensitivity of 0.17%/ε_r while necessitating only 30 μ of sample volume. In contrast, the dual-SRR sensor that has been proposed demonstrates a normalised permittivity sensitivity that is approximately 20 times greater, at 3.47%/ε_r, despite operating at a lower frequency of 4.15 GHz. Additionally, the proposed design provides a more comprehensive sensing capability by allowing simultaneous characterisation of both permittivity and permeability on solid substrates within a single compact structure, in contrast to the referenced sensor, which is restricted to single-parameter permittivity measurements of liquid samples.

4.4. Resonant Frequency Shift Behavior

This subsection presents measured S-parameter responses of the fabricated sensor and analyzes the resonant frequency shift behavior under different material loading conditions. The S_{21} was measured for both permittivity and permeability characterizations under unloaded conditions and with various MUTs placed on the sensing region. The resonant frequencies, denoted as the E-field (f_{re}) resonant frequency and H-field (f_{rm}) resonant frequency, were defined as the frequencies corresponding to the minimum magnitude of the S_{21} response and were consistently extracted from all the measurements.

Figure 9(a) shows S_{21} responses of the permittivity sensing structure unloaded and loaded with various substrate materials. Introduction of the MUT caused a clear downward shift in the resonant frequency, indicating strong coupling between the interdigital sensing region and the tested material. Materials with higher relative permittivity had a larger frequency shift due to increased effective capacitance in the electric-field-dominant sensing area. These resonant frequencies are representative of repeated experiment averages. Overall, these results confirm that the resonant behavior of the proposed sensor is primarily governed by electric-field interactions, which is consistent with the intended design. Fig. 9(b) shows the measured S_{21} responses of the permeability sensing structure for the same set of substrate materials.

Similar to permittivity studies, each MUT decreased the resonant frequency compared to the unloaded state. The given resonant frequencies are typical of the average results from numerous substrate tests, indicating the reproducibility of acceptable experimental data. The frequency shifts showed that the proposed sensor was sensitive to magnetic characteristics of the tested materials.

For all studied materials, the sensing structures' S_{21} responses were consistent. Fabrication tolerances, noise, and sample location error cause minor differences. The resonant frequencies are averaged to reduce these effects, yielding reproducible data for relative permittivity and permeability estimation.

4.5. Prediction Results

In Table 6, the relative permittivity and relative permeability values obtained using the mathematical models in Eqs. (3) and (4) are compared to the nominal values in the material datasheets to assess prediction accuracy. The projected permittivity and permeability values match the reference data for all substrate materials. To decrease random noise and sample-to-sample fluctuations, 10 independent measurements for each substrate were averaged to estimate resonant frequencies (f_{re} and f_{rm}). The substantial field confinement of the E-field and H-field sensing zones increased sensor sensitivity, resulting in reduced estimation errors across all materials.

The proposed sensor had a 3.07% average prediction error for permittivity characterization. Magtrex555 had the lowest forecast error of 0.03%, while Rogers Duroid 5870 had the biggest variation of 5.74%. Rogers Duroid 5870 has a low dielectric constant, resulting in a limited resonant frequency shift com-

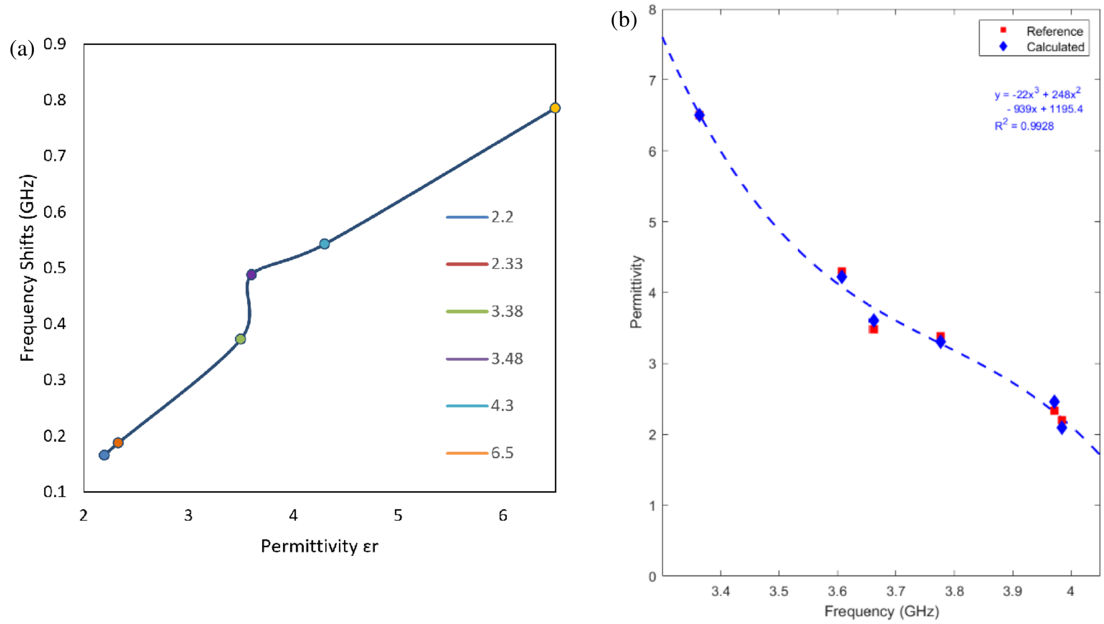

FIGURE 10. (a) Resonance frequency shift plot at various permittivity values and (b) comparison of permittivity between reference and prediction.

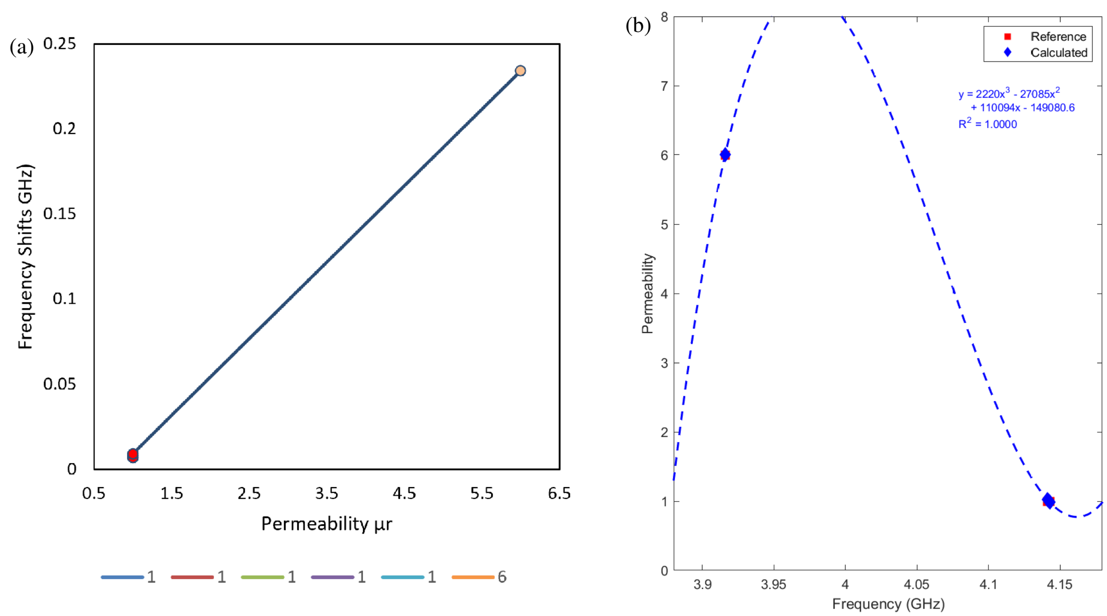

FIGURE 11. (a) Resonance frequency shift plot at various permeability values and (b) comparison of permeability between reference and calculation.

pared to materials with higher permittivity. Experimental uncertainties and the polynomial regression model used to correlate the resonant frequency with the MUT's dielectric properties affect prediction errors. Minor differences in the measured resonant frequency can affect derived permittivity values substantially. Higher permittivity materials cause larger resonant frequency shifts, which the sensor can detect more easily, improving prediction reliability. With an average error of 3.07% and a prediction accuracy of 96.93%, the suggested sensor can accurately characterize dielectrics.

For permeability characterization, FR4 had the highest prediction error of 2.66% and Magtrex555 the lowest at 0.03%. Due to its higher relative permeability than non-magnetic substrates, Magtrex555 has a more prominent resonant frequency shift and a more accurate prediction. Conversely, non-magnetic substrates with relative permeability close to unity cause only minor H-field perturbations in the SRR loop, resulting in smaller resonant frequency shifts and making the prediction process more susceptible to measurement uncertainties, though the errors remain within acceptable limits. All studied samples had an average permeability prediction error of 1.19% and an average prediction accuracy of 98.81%. These results show that the dual-parameter sensing approach can accurately characterize dielectric and magnetic properties using a single sensor platform.

TABLE 6. Comparison of nominal relative permittivity and permeability values with prediction results based on E-field and H-field distribution.

MUT	ε_r Reference	ε_r Prediction	%Error	μ_r Reference	μ_r Prediction	%Error
Rogers 5880	2.2	2.09	5.15	1	0.982	1.76
Rogers 5870	2.33	2.46	5.74	1	1.004	0.45
Rogers 4003C	3.38	3.31	2.13	1	1.004	0.45
Rogers 4350B	3.48	3.61	3.61	1	0.982	1.76
FR-4	4.3	4.22	1.77	1	1.027	2.66
Magtrex555	6.5	6.502	0.03	6	6.002	0.03

TABLE 7. Performance comparison of the proposed sensor with existing works.

Reference	Resonator	Measure Parameter	MUT	Working Frequency (GHz)	Sensitivity (MHz/unit)	%Sensitivity	%Error	Measurement (Range)
[27]	CSRR	Permittivity & Loss Tangent	Solid	2.0/5.41	150/480	7.48/8.51	N.R	1–2/2–10
[28]	Octagonal Spiral Resonators	Permittivity relative (ε_r)	Solid	2.48	114.3	4.61	< 2	2.25–4.5
[29]	Tweaking ELC Resonator	Permittivity relative (ε_r)	Solid	0.82	N.R	1.492	N.R	1–9.8
[30]	4-CRRRs-based SIW	Permittivity relative (ε_r)	Solid	3.1296/3.3636	N.R	6.33/6.17	0.5/0.9	2.1–2.8
[31]	Dual U-Shaped	Permittivity relative (ε_r)	Solid	1.21/2.1	N.R	N.R	N.R	2.2–4.3
[32]	Curve-Feed CSRR	Permittivity relative (ε_r)	Solid	2.5	1.072	N.R	0.23	1–4.4
[33]	Triple Ring CSRR	Permittivity relative (ε_r)	Solid	2.5	4.806	N.R	2.38/4	1–78.4
[34]	S-SRR + DSRR	Permittivity relative (ε_r)	Solid	5.122	N.R	3.27	N.R	1–4.3
[35]	TRB-CSRR	Permittivity relative (ε_r)+ thickness	Solid	4.86	N.R	32.72/12.94	0.2–3	1.006–12.9
[36]	CCRR	Permittivity relative (ε_r)	Solid	3.49	133	3.25	0.89	1–10
[37]	DSRR	Permittivity relative (ε_r)	Solid & Liquid	2.45	N.R	2.58/0.3	6.37/2.59	2.0–4.7
[13]	CMC-SRR	Permittivity relative (ε_r)+ thickness	Solid	17.39	N.R	8.05	7	2.2–10.2
[38]	SRR	Permittivity & Loss Tangent	Solid	2.5	N.R	0.687	1.18/3.91	2–3.2
This Work	SRR	Permittivity & Permeability	Solid	4.15	144.2/45.4	3.47/1.09	3.07/1.19	2.2–6.5/1–6

N.R, Result not reported in the original reference

The low prediction errors obtained for both permittivity and permeability confirm the effectiveness of the developed empirical models and validate the suitability of the proposed sensor for magneto-dielectric material characterization.

The low standard deviation obtained from the 60 measurements further verified the sensor's repeatability and measurement stability. Although the resolution among non-magnetic materials remains relatively limited owing to their nearly identical permeability values, the sensor successfully identifies the significant contrast between magnetic and non-magnetic materials, thereby validating its effectiveness for permeability characterization.

Figure 10(a) shows the correlation between MUT relative permittivity ε_r and resonant frequency shift (Δf). The resonant frequency shift grew monotonically with relative permittivity. It shows that the sensor responds consistently to dielectric fluctuations across the measuring range. Fig. 10(b) shows that the extracted permittivity values and datasheet references are correlated.

Figure 11(a) presents the permeability sensitivity plot, showing the relationship between relative permeability (μ_r) and resonant frequency shift (Δf_r). The non-magnetic substrates $(\mu_r = 1)$ produce closely clustered and relatively small frequency shifts, while the magnetic material $(\mu_r = 6)$ exhibits a clearly higher response. Fig. 11(b) shows the extracted permeability values together with their corresponding reference data.

Table 7 indicates that most recently reported microwave sensors primarily focus on permittivity characterization, whereas the proposed design enables extraction of both the relative permittivity and relative permeability using a single resonator.

Despite its relatively simple SRR-based configuration, the proposed sensor achieves competitive sensitivities of 144.2 MHz/ε_r and 45.4 MHz/μ_r, while maintaining low measurement errors of 3.07% and 1.19% for permittivity and permeability, respectively. These findings demonstrate the effectiveness of the proposed approach for dual-parameter characterization, offering reliable measurement performance.

5. CONCLUSION

This work successfully demonstrates that the spatial segregation of electric-field- and magnetic-field-dominated sensing mechanisms via a dual-SRR architecture enables independent extraction of relative permittivity and relative permeability. The proposed sensor offers a robust, low-cost, and non-destructive solution for magnetodielectric characterization. Experimental results from 60 independent measurements confirm high reliability, achieving average accuracies of 96.93% and 98.81% for permittivity and permeability, respectively. The sensor's ability to maintain a minimum error of 0.03% for complex magnetodielectric materials like Magtrex555 highlights its superior decoupled sensing capability compared to traditional multi-mode configurations.

Future research may explore the characterization of additional magnetic and magnetodielectric materials covering a wider permeability range to further validate the sensor's versatility. Moreover, optimization of the sensing structure to suppress residual coupling between the electric-field and magnetic-field regions, together with improvements in sample placement accuracy and calibration procedures, represents a promising direction for enhancing measurement performance. The proposed sensing approach could also be implemented at different operating frequencies to extend its applicability to various microwave characterization requirements.

ACKNOWLEDGEMENT

The authors would like to thank the Universitas Riau for facilitating the research collaboration with the Research Center for Telecommunication, National Research and Innovation Agency (BRIN).

REFERENCES

[1] Rahman, N. A., Z. Zakaria, R. A. Rahim, Y. Dasril, and A. A. M. Bahar, "Planar microwave sensors for accurate measurement of material characterization: A review," *TELKOMNIKA (Telecommunication Computing Electronics and Control)*, Vol. 15, No. 3, 1108–1118, 2017.

[2] Jilani, M. T., A. M. Khan, M. T. Khan, S. M. Ali, *et al.*, "A brief review of measuring techniques for characterization of dielectric materials," *International Journal of Information Technology and Electrical Engineering*, Vol. 1, No. 1, 1–5, 2012.

[3] Canova, A., M. Quercio, and L. Solimene, "Magnetic characterisation of ferromagnetic material," *e-Journal of Nondestructive Testing*, Vol. 29, No. 6, Jun. 2024.

[4] Kumar, S., S. Middha, S. Masih, A. Kaur, J. Pal, N. Alhokbany, J. Ahmed, G. Singh, S. Singh, N. Tandon, *et al.*, "Magneto-dielectric composites synthesized using industrial waste," *Journal of Magnetism and Magnetic Materials*, Vol. 629, 173306, 2025.

[5] Nelson, S. O. and S. Trabelsi, "Use of material dielectric properties for agricultural applications," in *2016 ASABE Annual International Meeting*, Orlando, Florida, USA, Jul. 2016.

[6] Das, S., M. M. Das, P. Dhamodharan, and C. Manoharan, "Dielectric, magnetic and electrochemical characterization of $CoFe_2O_4$ nanoparticles and their application as an anode material in Li-ion battery," *Inorganic Chemistry Communications*, Vol. 145, 110050, 2022.

[7] Tipsawat, P., U. Wongpratat, S. Phumying, N. Chanlek, K. Chokprasombat, and S. Maensiri, "Magnetite (Fe_3O_4) nanoparticles: Synthesis, characterization and electrochemical properties," *Applied Surface Science*, Vol. 446, 287–292, 2018.

[8] Bagheri Hosseinabadi, M., N. Khanjani, M. H. Ebrahimi, B. Haji, and M. Abdolahfard, "The effect of chronic exposure to extremely low-frequency electromagnetic fields on sleep quality, stress, depression and anxiety," *Electromagnetic Biology and Medicine*, Vol. 38, No. 1, 96–101, 2019.

[9] Li, X. Y., L. Chen, Z. X. Cai, K. Z. Zhao, Q. Ma, J. W. You, and T. J. Cui, "Contactless electromagnetic human sensing for biomedical and healthcare applications (Invited Review)," *Progress In Electromagnetics Research*, Vol. 182, 121–139, 2025.

[10] Roslan, H. S., M. A. M. Said, Z. Zakaria, and M. H. Misran, "Recent development of planar microwave sensor for material characterization of solid, liquid, and powder: A review," *Bulletin of Electrical Engineering and Informatics*, Vol. 11, No. 4, 1911–1918, 2022.

[11] Alam, T. and M. Cheffena, "Integrated microwave antenna/sensor for sensing and communication applications," *IEEE*

Transactions on Microwave Theory and Techniques, Vol. 70, No. 11, 5289–5300, 2022.

[12] Adhiyoga, Y. G., S. F. Rahman, C. Apriono, and E. T. Rahardjo, "Miniaturized 5G antenna with enhanced gain by using stacked structure of split-ring resonator array and magnetodielectric composite material," *IEEE Access*, Vol. 10, 35 876–35 887, 2022.

[13] Haq, T. and S. Koziel, "Novel complementary multiple concentric split ring resonator for reliable characterization of dielectric substrates with high sensitivity," *IEEE Sensors Journal*, Vol. 24, No. 10, 16 233–16 241, 2024.

[14] Amer, R. A. B., N. A. Shairi, M. A. M. Said, Z. Zakaria, M. H. Misran, A. Othman, S. Alam, and S. K. A. Rahim, "Single-port microwave sensor using defected ground structure complementary split ring resonator for solid material characterization," *Progress In Electromagnetics Research C*, Vol. 158, 139–149, 2025.

[15] Murali, V. P., J. Joseph, and K. Ostrikov, "Electromagnetic field sensors," in *Advanced Materials for Electromagnetic Shielding: Fundamentals, Properties, and Applications*, 35–60, Chapter 3, M. Jaroszewski, S. Thomas, A. V. Rane (eds.), Wiley, 2018.

[16] Ismail, M. K., Z. Zakaria, N. Hassan, S. W. Yik, and M. M. Abdullah, "Microwave planar sensor for determination of the permittivity of dielectric material," *Bulletin of Electrical Engineering and Informatics*, Vol. 7, No. 4, 640–649, 2018.

[17] Ibrahim, M., R. A. Rahim, J. M. Nordin, S. Zulaika, A. Nyzam, and N. A. Amatkhri, "Dielectric properties characterization of the rice and rice weevil for microwave heating treatment," *Indonesian Journal of Electrical Engineering and Computer Science*, Vol. 13, No. 2, 752–758, 2019.

[18] Famoriji, O. J. and T. Shongwe, "Transmission line characterization and modeling for electronic circuits and systems design," *Indonesian Journal of Electrical Engineering and Computer Science*, Vol. 30, No. 2, 730–738, May 2023.

[19] Navaei, M., P. Rezaei, and S. Kiani, "Measurement of low-loss aqueous solutions permittivity with high detection accuracy by a contact and free-label resonance microwave sensor," *International Journal of Communication Systems*, Vol. 36, No. 5, e5417, Mar. 2023.

[20] Navaei, M., P. Rezaei, and S. Kiani, "A symmetric bar chart-shape microwave sensor with high Q-factor for permittivity determination of fluidics," *International Journal of Microwave and Wireless Technologies*, Vol. 15, No. 8, 1334–1342, 2023.

[21] Shafi, K. T. M., M. A. H. Ansari, A. K. Jha, and M. J. Akhtar, "Design of SRR-based microwave sensor for characterization of magnetodielectric substrates," *IEEE Microwave and Wireless Components Letters*, Vol. 27, No. 5, 524–526, 2017.

[22] Wang, Y.-R. and H. Hao, "Design of a microstrip sensor based on a CSRR-derived structure for measuring the permittivity and permeability of materials," *Progress In Electromagnetics Research M*, Vol. 111, 235–246, 2022.

[23] Saadat-Safa, M., V. Nayyeri, M. Khanjarian, M. Soleimani, and O. M. Ramahi, "A CSRR-based sensor for full characterization of magneto-dielectric materials," *IEEE Transactions on Microwave Theory and Techniques*, Vol. 67, No. 2, 806–814, 2019.

[24] Boybay, M. S. and O. M. Ramahi, "Material characterization using complementary split-ring resonators," *IEEE Transactions on Instrumentation and Measurement*, Vol. 61, No. 11, 3039–3046, Nov. 2012.

[25] Raveendran, A. and S. Raman, "Low cost multifunctional planar RF sensors for dielectric characterization and quality monitoring," *IEEE Sensors Journal*, Vol. 21, No. 21, 24 056–24 065, Nov. 2021.

[26] Navaei, M., P. Rezaei, and S. Kiani, "Microwave split ring resonator sensor for determination of the fluids permittivity with measurement of human milk samples," *Radio Science*, Vol. 57, No. 7, 1–11, Jul. 2022.

[27] Liu, X., D. Zhang, S. Yu, C. Wang, X. Yang, and Y. Wang, "A dual-band resonator sensor for low permittivity characterization," *IEEE Transactions on Instrumentation and Measurement*, Vol. 71, 1–11, 2022.

[28] Liu, Q., H. Deng, P. Meng, and H. Sun, "High sensitivity sensor loaded with octagonal spiral resonators for retrieval of solid material permittivity," *IEEE Sensors Journal*, Vol. 21, No. 18, 20 010–20 017, Sep. 2021.

[29] Alam, S., I. Surjati, L. Sari, Y. K. Ningsih, M. Y. Fathanah, Y. K. Gultom, G. Daffin, T. Firmansyah, and Z. Zakaria, "UHF-band solid sensor based on tweaking electric field coupled resonator for material characterization," *Progress In Electromagnetics Research M*, Vol. 126, 11–18, 2024.

[30] Wu, W.-J., L. Shang, W.-S. Zhao, and G. Wang, "A dual-mode microwave sensor for retrieving permittivity of materials based on multiple complementary rectangular ring resonators," *Measurement*, Vol. 218, 113215, 2023.

[31] Alam, S., Z. Zakaria, I. Surjati, N. A. Shairi, M. Alaydrus, and T. Firmansyah, "Highly independent dual-band permittivity sensors for simultaneous measurement of solid materials," in *2023 33rd International Conference Radioelektronika (RADIOELEKTRONIKA)*, 1–4, Pardubice, Czech Republic, 2023.

[32] Al-Gburi, A. J. A., Z. Zakaria, N. A. Rahman, S. Alam, and M. A. M. Said, "A compact and low-profile curve-feed complementary split-ring resonator microwave sensor for solid material detection," *Micromachines*, Vol. 14, No. 2, 384, Feb. 2023.

[33] Al-Gburi, A. J. A., N. A. Rahman, Z. Zakaria, and M. Palandoken, "Detection of semi-solid materials utilizing triple-rings CSRR microwave sensor," *Sensors*, Vol. 23, No. 6, 3058, Mar. 2023.

[34] Masrakin, K., S. Z. Ibrahim, H. A. Rahim, S. N. Azemi, P. J. Soh, and S. Tantiviwat, "Microstrip sensor based on ring resonator coupled with double square split ring resonator for solid material permittivity characterization," *Micromachines*, Vol. 14, No. 4, 790, 2023.

[35] Singh, K. K., A. K. Singh, S. K. Mahto, R. Sinha, and A. J. A. Al-Gburi, "Enhanced accuracy and high sensitivity in dielectric characterization through a compact and miniaturized metamaterial inspired microwave sensor," *Sensors and Actuators A: Physical*, Vol. 370, 115271, May 2024.

[36] Han, X., X. Li, Y. Zhou, Z. Ma, P. Peng, C. Fu, and L. Qiao, "Microwave sensor loaded with complementary curved ring resonator for material permittivity detection," *IEEE Sensors Journal*, Vol. 22, No. 21, 20 456–20 463, Nov. 2022.

[37] Jang, S.-Y. and J.-R. Yang, "Double split-ring resonator for dielectric constant measurement of solids and liquids," *Journal of Electromagnetic Engineering and Science*, Vol. 22, No. 2, 122–128, 2022.

[38] Huq, S. M. I., G. Xiao, and S. Bhadra, "Printed split ring resonator based microwave sensor on biodegradable substrate for dielectric characterization," *Sensors and Actuators A: Physical*, Vol. 393, 116856, 2025.